

# ELECTRONIC SUPPLEMENTARY INFORMATION

## Comparison of arsenate adsorption from neutral pH aqueous solutions using two different iron-trimesate porous solids: kinetics, equilibrium isotherms, and synchrotron X-ray absorption experiments

Eliana Berardozi<sup>1</sup>, Jimena S. Tuninetti<sup>1</sup>, Fernando S. García Einschlag<sup>1</sup>, Omar Azzaroni<sup>1</sup>, Marcelo Ceolín<sup>1,\*</sup>, and Matías Rafti<sup>1,\*\*</sup>

<sup>1</sup>Instituto de Investigaciones Físicoquímicas Teóricas y Aplicadas (INIFTA), Departamento de Química, Facultad de Ciencias Exactas, Universidad Nacional de La Plata (UNLP), CONICET, (1900) La Plata, Argentina

\* mceolin@inifta.unlp.edu.ar, \*\* mrafti@quimica.unlp.edu.ar

This supporting information contains 12 pages, including detailed information on the techniques used, and 8 figures for complementary characterization of synthesized materials: wide angle x-ray scattering (WAXS), transmission electron microscopy (TEM), vibrational spectroscopy (FTIR), TGA, and x-rays absorption spectroscopy (XAS).

## **1. Procedures and equations for adsorption isotherms and kinetics.**

Both, arsenic mass loading on the porous adsorbent materials (mg/g) and removal percentage from the initial solutions used (%) were obtained using Equations 1 and 2,

$$q_t = \frac{C_0 - C_t}{\left(\frac{m}{V}\right)} \quad \text{Equation 1}$$

$$Re = \frac{C_0 - C_t}{C_0} * 100 \quad \text{Equation 2}$$

where  $q_t$  is the amount of arsenic loaded (mg/g),  $C_0$  is the initial As(V) concentration in the solution (mg/L),  $C_t$  is the concentration at time  $t$  in the solution (mg/L),  $V$  is the volume (L),  $M$  is the porous material dose (g) and  $Re$  the removal percentage (%).

## **2. Equilibrium adsorption isotherms and adsorption kinetics.**

Langmuir isotherm model assumes monolayer adsorption over uniformly distributed active sites with identical affinity towards the adsorbate, which once occupied cannot participate in further adsorption events. One of the most useful parameters that can be extracted from the Langmuir treatment is the so-called adsorbent saturation capacity, which corresponds to the extrapolation of adsorbate loading for maximum concentration limit values. On the other hand, Freundlich model isotherm allows for description of surfaces having heterogeneously distributed energies for adsorption sites and, in contrast with the Langmuir model, there is no loading saturation in the high concentration limit, nor the equation reduces to Henry's law for the low concentration limit. The linearized Langmuir and Freundlich equations, which were used for fitting experimental data are presented below (Equations 3 and 4):

$$\frac{C_e}{q_e} = \frac{1}{q_m K_L} + \frac{C_e}{q_m} \quad \text{Equation 3}$$

$$\ln \ln q_e = \frac{1}{n} \ln \ln C_e - \ln \ln K_F \quad \text{Equation 4}$$

where,  $C_e$  is the adsorbate equilibrium concentration (mg/L),  $q_e$  is the adsorbed quantity per adsorbent unit mass (mg/g),  $K_L$  is the Langmuir constant (L/mg),  $q_m$  is the theoretical monolayer saturation capacity (mg/g), and  $K_F$  and  $n$  are the Freundlich constants, which

are proportional to the adsorption capacity and the adsorbent adsorption energy, respectively.

Concentration time evolution for the time span between 0.15 and 48 hours was followed using different adsorbent amounts (16, 100, and 400 mg/L), and initial arsenic concentrations of 0.2 mg/L with fixed pH = 7.0. The solids obtained after established adsorption equilibrium were washed and dried for further characterization.

$$q(t) = q_e(1 - \exp(-k_1 * t)) \quad (\text{pseudo-first order}) \quad \text{Equation 5}$$

$$\frac{t}{q_t} = \frac{1}{k_2 q_e^2} + \frac{1}{q_e} * t \quad (\text{pseudo-second order}) \quad \text{Equation 6}$$

Generally speaking, adsorption in a porous solid involves three sequential steps: (i) transport of the adsorbate from bulk solution to adsorbent particle external surface (film transport), (ii) transport of the adsorbate within the pore network present on the adsorbent particle (intra-particle diffusion), and (iii) adsorption on the active site on the adsorbent pore wall surface. Since the relative importance of each step may depend both on, operating conditions (such as mixing speed, temperature and adsorbate concentration) and adsorbent characteristics (such as particle size, adsorption energies and surface area); simple models would naturally give only a rough description for the uptake rate.

### **3. Characterization techniques used**

**Vibrational spectroscopy (FTIR).** Vibrational spectra of initial and Arsenic-exposed MOFs were obtained in order to gain insight interactions dominating the adsorption process. Measurements were carried with a FTIR-Varian 660 infrared spectrometer using single-point ATR configuration with a ZnSe crystal.

**X-ray diffraction (WAXS).** Crystalline structure of initial and As-exposed MOFs were studied using wide angle X-ray scattering (WAXS). The SAXS/WAXS system (INIFTA, project “Nanopymes”, EuropeAid/132184/D/SUP/AR-Contract 331–896) is a XEUSS 1.0 HR (XENOCSS, Grenoble) equipped with a microfocus X-ray source and a Pilatus 100 K detector (DECTRIS AG, Switzerland).

**ICP and XPS experiments.** Arsenic was determined using a surface sensitive technique, X-ray Photoelectron Spectroscopy (XPS), and a bulk-averaged technique, Ion Coupled Plasma Spectroscopy (as performed on pre-digested liquid samples). XPS experiments were carried in a SPECS Sage HR 100 spectrometer equipped with non-monochromatic X-ray source (Aluminum  $K\alpha$  line of 1486.6 eV energy and 300 W); while ICP experiments were carried in a ICP-MS (iCAP-Q, Thermo) Inductively coupled plasma mass spectrometer equipped with collision/reaction cell and Kinetic Energy Discrimination (KED) that allowed to remove most of isobaric interferences that can affect to the limit of detection of several elements.

**Thermogravimetric Analysis (TGA).** Experiments for the evaluation of thermal stability of the solids after Arsenic adsorption were carried on a Q-500 TA apparatus under 40 mL/min  $N_2$  flow at a 10 K/min temperature ramp.

**Transmission Electron Microscopy (TEM).** Experiments for the evaluation of size and morphology of Fe-BTC synthesized materials were carried using a JEM 1200EX II (Jeol) apparatus.

**X-ray absorption experiments and modelling.** EXAFS/XANES experiments were carried at the D08B-XAFS2 beam line of the Laboratório Nacional de Luz Síncrotron (CNPEM-LNLS, Campinas, Brazil). All the experiments were performed in transmission mode using ionization chambers as photon detectors. All the experiments were performed at 22 °C. Every spectrum was obtained as the average of, at least, three individual runs. Real-time energy calibration was achieved using an iron foil (Fe  $K$ -edge, at 7112 eV) and a gold foil ( $Au^0$   $L_3$ -edge at 11919 eV, for As  $K$ -edge). Spectra pre-processing, and model

fitting and scattering path calculation was done using the routines coded in the DEMETER suite.<sup>1</sup> Local structure corresponding to Ferric-acetate (Fe K-edge) and sodium Arsenate(V) (As K-edge) were used as suitable models for scattering path calculations.<sup>2</sup>

#### **4. FTIR characterization.**

Spectra taken on powder samples prepared with dried F-300 adsorbent before and after exposure to 80 ppm As(V) solutions are depicted in Figure S1. Results clearly show the appearance of new absorption intense features centered at  $794\text{ cm}^{-1}$  attributable to As-O or Fe-O-As vibrational, and  $660\text{ cm}^{-1}$  corresponding to asymmetrical As-O stretching modes.<sup>3,4</sup> Conditions used for the exposure are identical to those described in the adsorption experiments protocol (see manuscript section 2.3). Briefly, solutions were prepared from stock solutions of As(V) as arsenate ( $\text{AsO}_4^{3-}$ ) 500.0 ppm concentration, and adjusted to pH=7.0. Also, it can be mentioned the appearance of a mild feature centered at  $1750\text{ cm}^{-1}$ , which may be assigned to C=O stretching on the BTC linker.

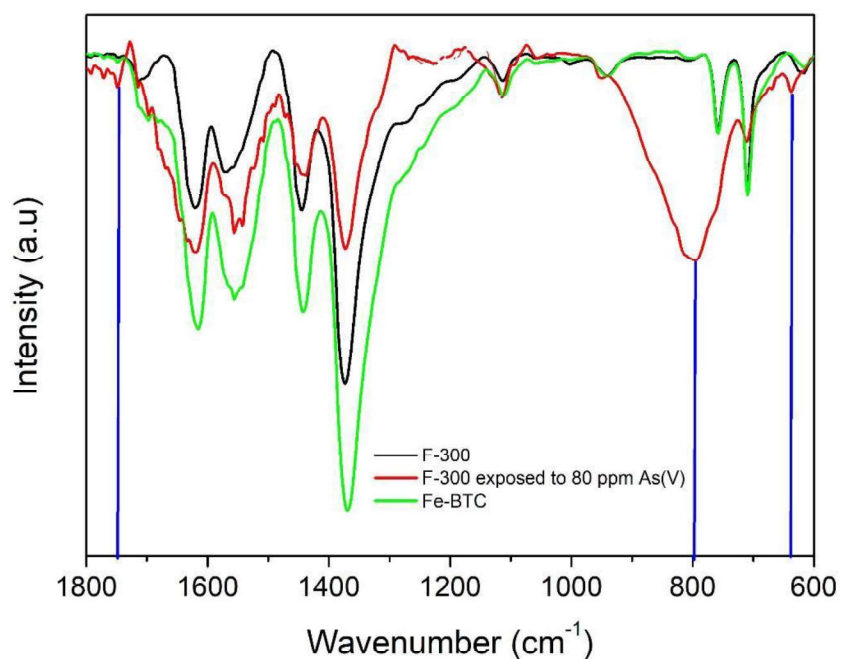


**Figure S1.** FTIR spectra from F-300 solid both after and before exposure to As(V) solutions.

## 5. Adsorption experiments and comparison with benchmark materials.

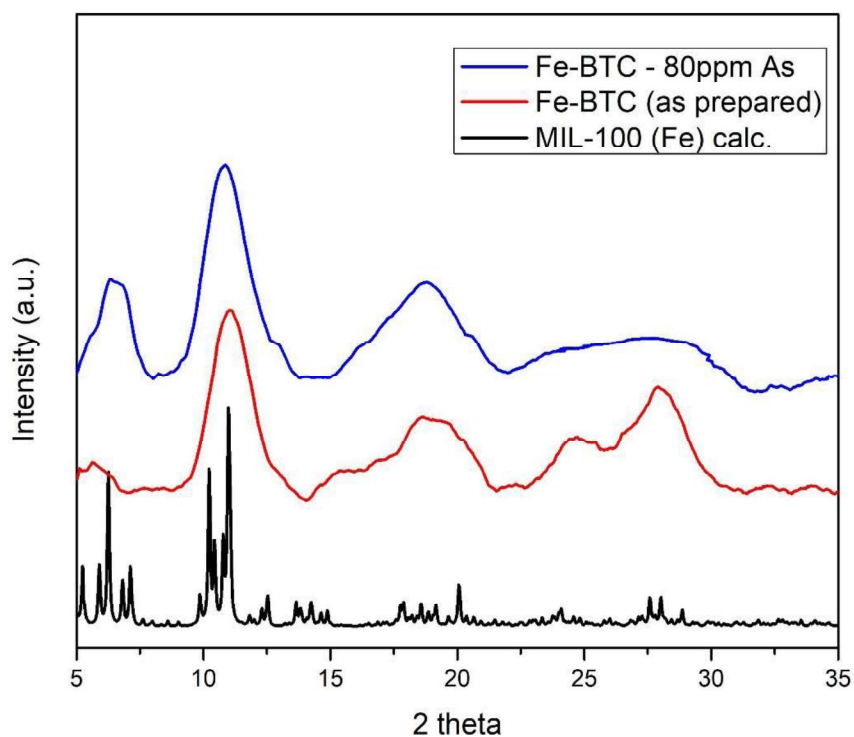
See table S1 were different materials and performances are compared for Arsenic adsorption.<sup>5</sup>

**Table S1.** Comparison between different Arsenic loadings achieved with iron-based materials in the recent literature.

Material	Adsorption capacity (mg As/g solid)	Adsorption capacity (mg As/g Fe)	REFERENCE
F-300	165.32 mg As/g	776.32 mg As/g Fe	This work
Fe/Mg-MIL-88B(0.5)	303.6 mg As/g		Gu, Y., Xie, D., Wang, Y., Qin, W., Zhang, H., Wang, G., ... & Zhao, H. (2019). Facile fabrication of composition-tunable Fe/Mg bimetal-organic frameworks for exceptional arsenate removal. <i>Chemical Engineering Journal</i> , 357, 579-588. <a href="https://doi.org/10.1016/j.cej.2018.09.174">https://doi.org/10.1016/j.cej.2018.09.174</a>
MOF-808	24.83 mg As/g		Li, Z., Yang, J., Sui, K., & Yin, N. (2015). Facile synthesis of metal-organic framework MOF-808 for arsenic removal. <i>Materials Letters</i> , 160, 412-414. <a href="https://doi.org/10.1016/j.matlet.2015.08.004">https://doi.org/10.1016/j.matlet.2015.08.004</a>
Zn MOF UiO-66	147.71 mg As/g		Wang, C., Liu, X., Chen, J. P., & Li, K. (2015). Superior removal of arsenic from water with zirconium metal-organic framework UiO-66. <i>Nature Publishing Group</i> , 1-10. <a href="https://doi.org/10.1038/srep16613">https://doi.org/10.1038/srep16613</a>
RT-Zn-MOF-74	99 mg As/g		Tarboush, B. J. A., Chouman, A., Jondenan, A., Ahmad, M., Hmadeh, M., & Al-ghoul, M. (2018). Metal Organic Framework-74 for Ultra-Trace Arsenic Removal from Water: Experimental and Density Functional Theory Studies. <a href="https://doi.org/10.1021/acsanm.8b00501">https://doi.org/10.1021/acsanm.8b00501</a>
HT-Zn-MOF-74	48.7 mg As/g		Tarboush, B. J. A., Chouman, A., Jondenan, A., Ahmad, M., Hmadeh, M., & Al-ghoul, M. (2018). Metal Organic Framework-74 for Ultra-Trace Arsenic Removal from Water: Experimental and Density Functional Theory Studies. <a href="https://doi.org/10.1021/acsanm.8b00501">https://doi.org/10.1021/acsanm.8b00501</a>
Peerles iron	0.38 mg As/g	0.42 mg As/g Fe	Su, C., & Puls, R. W. (2003). In situ remediation of arsenic in simulated groundwater using zerovalent iron: Laboratory column tests on combined effects of phosphate and silicate. <i>Environmental Science and Technology</i> , 37(11), 2582-2587. <a href="https://doi.org/10.1021/es026351q">https://doi.org/10.1021/es026351q</a>
Natural laterite	0.565 mg As/g	1.20 mg As/g Fe	Maiti, A., DasGupta, S., Basu, J. K., & De, S. (2008). Batch and column study: Adsorption of arsenate using untreated laterite as adsorbent. <i>Industrial and Engineering Chemistry Research</i> , 47(5), 1620-1629. <a href="https://doi.org/10.1021/ie070908z">https://doi.org/10.1021/ie070908z</a>
	0.736 mg As/g		Maiti, A., Sharma, H., Basu, J. K., & De, S. (2009). Modeling of arsenic adsorption kinetics of synthetic and contaminated groundwater on natural laterite. <i>Journal of Hazardous Materials</i> , 172(2-3), 928-934. <a href="https://doi.org/10.1016/j.jhazmat.2009.07.140">https://doi.org/10.1016/j.jhazmat.2009.07.140</a>
Iron Filings (Zero-valent Iron)	4.4 mg As/g	4.90 mg As/g Fe	Nikolaidis, N. P., Dobbs, G. M., & Lackovic, J. (2003). Arsenic removal by zero-valent iron: field, laboratory and modeling studies. <i>Water Research</i> , 37(6), 1417-1425. <a href="https://doi.org/10.1016/S0043-1354(02)00483-9">https://doi.org/10.1016/S0043-1354(02)00483-9</a>
	0.6 mg As/g		Doherty, L., & Observatory, E. (2005). Removal of Methylated Arsenic in Groundwater with Iron Filings. <i>Water Research</i> , 39(19), 7662-7666.
	45 mg As/g	47.37 mg As/g Fe	Bang, S., Korfiatis, G. P., & Meng, X. (2005). Removal of arsenic from water by zero-valent iron. <i>Journal of Hazardous Materials</i> , 121(1-3), 61-67. <a href="https://doi.org/10.1016/j.jhazmat.2005.01.030">https://doi.org/10.1016/j.jhazmat.2005.01.030</a>
Granular ferric hydroxide	8 mg As/g		Badruzzaman, M., Westerhoff, P., & Knappe, D. R. U. (2004). Intraparticle diffusion and adsorption of arsenate onto granular ferric hydroxide (GFH). <i>Water Research</i> , 38(18), 4002-4012. <a href="https://doi.org/10.1016/j.watres.2004.07.007">https://doi.org/10.1016/j.watres.2004.07.007</a>

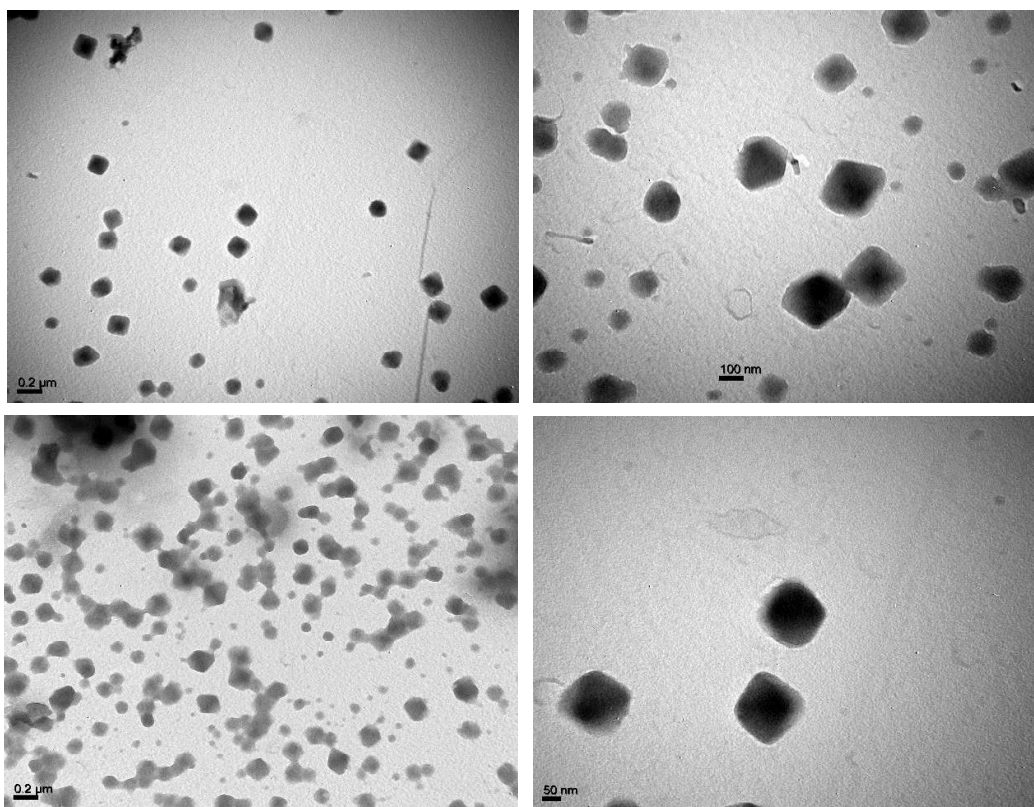
## **6. Structural and chemical characterization using WAXS, TEM and X-ray absorption experiments.**

Figure S2 shows WAXS experiments for comparison of the structure of Fe-BTC (both after and before exposure to As(V) solutions) with MIL-100 (Fe) calculated diffractogram obtained from reported crystalline structure.



**Figure S2.** Comparison between diffraction patterns obtained for Fe-BTC porous solids versus MIL-100(Fe), both after and before exposure to 80 ppm As(V) aqueous solutions

In Figure S3 TEM images of Fe-BTC materials featuring octahedral morphologies can be observed. The size distribution presents some polydispersity, although this might be expected due to the lack of HF directing agent in the synthesis.



**Figure S3.** Transmission Electron Microscopy images of as prepared Fe-BTC material at different magnifications.

In Figure S4, EXAFS experiments corresponding to a comparison between Fe-BTC porous materials exposed to 0.2 ppm to 80 ppm As(V) solutions are displayed. Arsenic K-edge XANES experiments corresponding to reference materials featuring As(III) and As(V) oxidation states, and both F-300 and Fe-BTC after exposure to 80 ppm As(V) stock solutions were compared (Figure S5). It is clear that no As(III) is present on the adsorbed phase, thus ruling out the possibility of adsorptive reduction, as both Fe-BTC and F-300 samples feature peaks centered virtually at the same energy values. The EXAFS signals obtained for Arsenic in both F-300 and Fe-BTC porous materials can be observed in Figure S6.

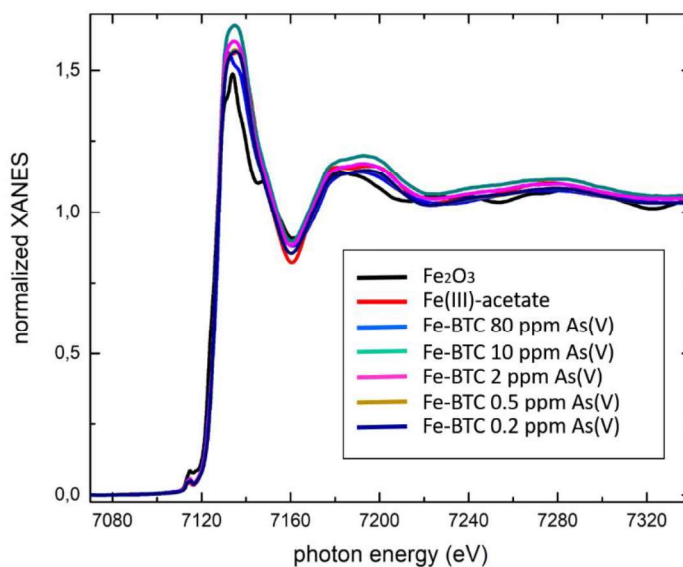
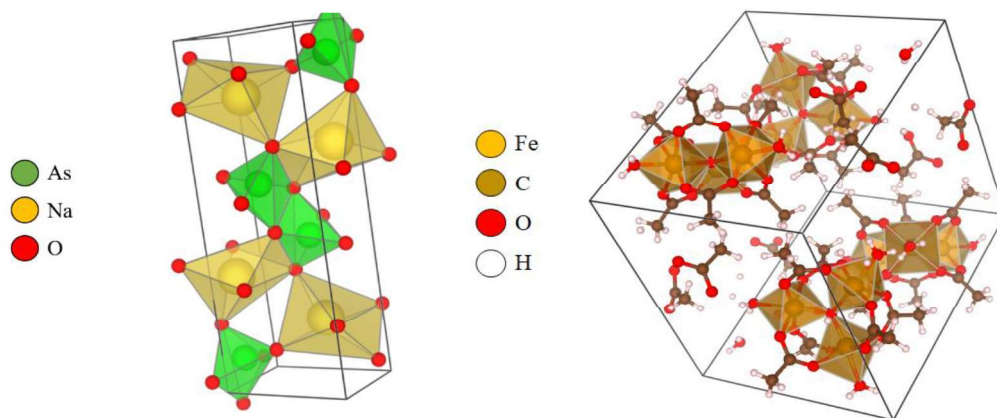


**Figure S4.** Iron K-edge XANES experiments of Fe-BTC samples loaded with increasingly higher Arsenic amounts and a its comparison with both Fe(III) acetate and oxide standards.



**Scheme S1.** Model structures used for the environment of (left) Arsenic and (right) Iron atoms on the porous support.

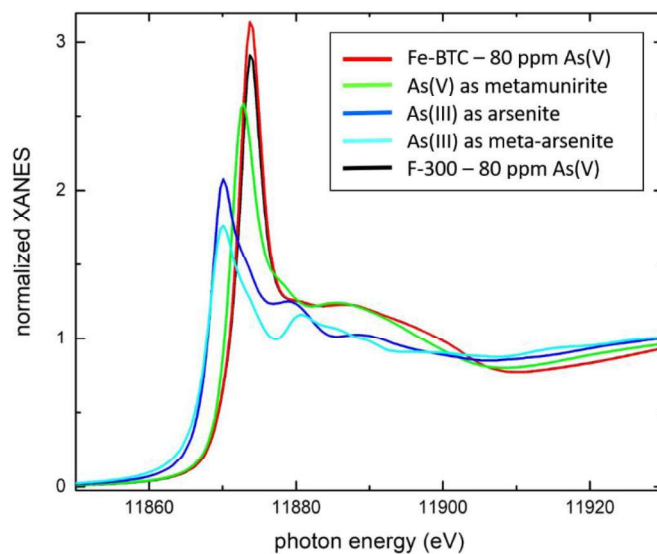


**Figure S5.** Arsenic K-edge XANES experiments. Both Fe-BTC and F-300 porous samples loaded with 80 ppm As (V) do not show significant differences.

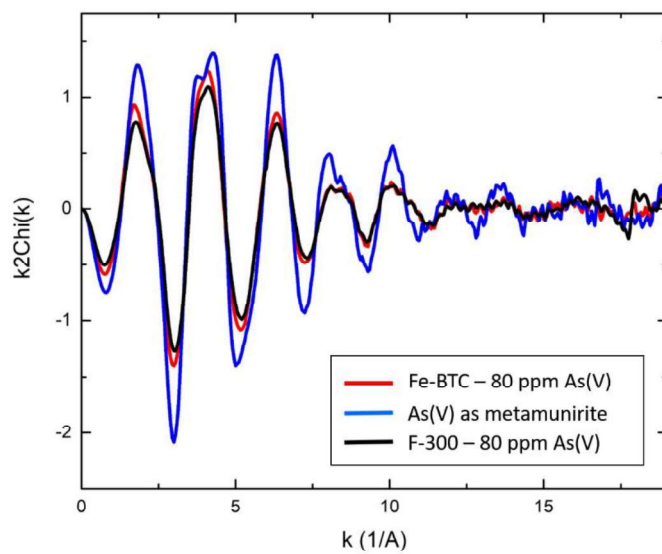


**Figure S6.** Arsenic K-edge EXAFS experiments for both F-300 and Fe-BTC porous solids loaded with 80 ppm As(V). Modelling shows no significant differences between both materials.

In figure S7, TGA experiments performed using different arsenic loadings and the effect on residual percentage at high temperatures can be observed. The most significant weight loss event in the As(V)-containing sample (after dehydration) occurs at 160 °C, and can be used as an indication of adsorbate loading in the Fe-BTC sample after exposure. As expected from the observed high temperature residue (approx. 60%) on the bare arsenate salt thermogram, As(V)-exposed Fe-BTC samples feature an increased  $\approx 50\%$  high temperature residue compared to the  $\approx 20\% - 30\%$  observed for bare Fe-BTC.

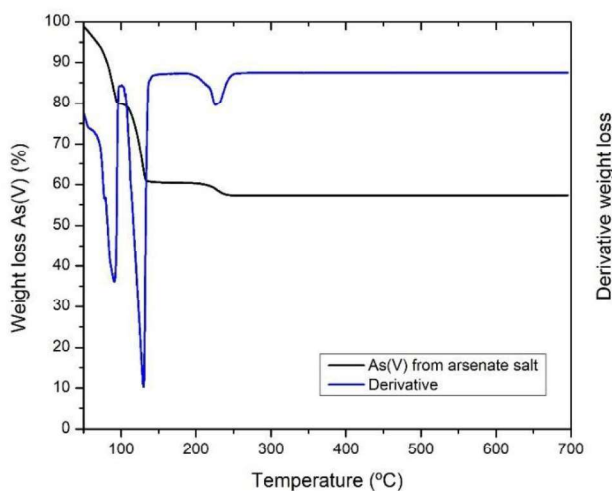
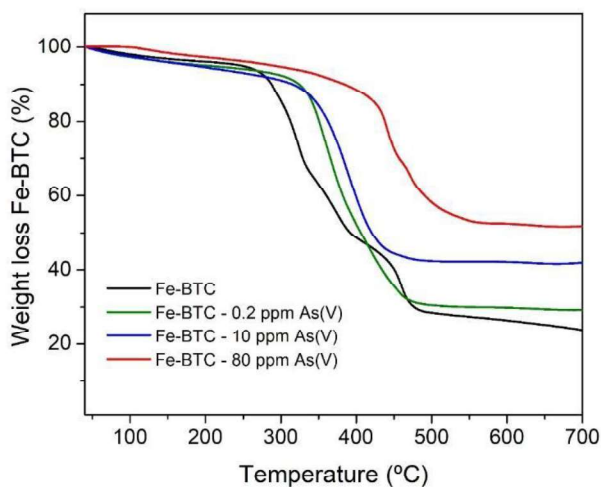


**Figure S7 (top).** The effect of increasingly higher amounts of Arsenic on Fe-BTC on the porous support thermal behavior. **(bottom)** Thermal decomposition profiles for As(V)-containing salt used ( $\text{HN}_2\text{AsO}_4 \cdot 7\text{H}_2\text{O}$ ).

## Bibliography

- 1 B. Ravel and M. Newville, *J. Synchrotron Radiat.*, 2005, **12**, 537–541.
- 2 S. Yao, J. Liu and Q. Han, *Acta Crystallogr. Sect. E Struct. Reports Online*, , DOI:10.1107/S1600536808019806.
- 3 J. W. Jun, M. Tong, B. K. Jung, Z. Hasan, C. Zhong and S. H. Jhung, *Chem. - A Eur. J.*, 2015, **21**, 347–354.
- 4 S. Huang, K. L. Yang, X. F. Liu, H. Pan, H. Zhang and S. Yang, *RSC Adv.*, 2017, **7**, 5621–5627.
- 5 C. Wang, J. Luan and C. Wu, *Water Res.*, 2019, **158**, 370–382.